On Closure Phase and Systematic Bias in Multi-looked SAR Interferometry

Yujie Zheng, Heresh Fattahi, Piyush Agram, Mark Simons, and Paul Rosen

***Abstract*—In this article, we investigate the link between closure phase and the observed systematic bias in deformation modeling with multi-looked SAR interferometry. Multi-looking or spatial averaging is commonly used to reduce stochastic noise over a neighborhood of distributed scatterers in InSAR measurements. However, multi-looking may break consistency among a triplet of interferometric phases formed from three acquisitions leading to a residual phase error called closure phase. Understanding the cause of closure phase in multi-looked InSAR measurements and the impact of closure phase errors on the performance of InSAR time-series algorithms is crucial for quantifying the uncertainty of ground displacement time-series derived from InSAR measurements. We develop a model that consistently explains both closure phase and systematic bias in multi-looked interferometric measurements. We show that non-zero closure phase can be an indicator of temporally inconsistent physical processes that alter both phase and amplitude of interferometric measurements. We propose a method to estimate the systematic bias in the InSAR time-series with generalized closure phase measurements. We validate our model with a case study in Barstow-Bristol trough, California. We find systematic differences on the order of cm/year between InSAR time-series results using subsets of varying maximum temporal baseline. We show that these biases can be identified and accounted for.**

***Index Terms*—InSAR, InSAR time-series, Phase Consistency, Closure Phase, Systematic Bias**

I. Introduction

INTERFEROMETRIC Synthetic Aperture Radar (InSAR) time-series analysis is an established Earth remote sensing technique for monitoring temporal changes of the Earth surface displacements. InSAR has been used to study a variety of phenomena including volcanic inflation and deflation, landslides, tectonic deformation across faults, seismic and aseismic fault slip and groundwater-induced deformation [1]–[8]. InSAR time-series algorithms exploit interferogram stacks to reduce the impact of uncorrelated or partially correlated noise in individual InSAR measurements, such as signal decorrelation [9], [10] and atmospheric delay [11], [12].

InSAR measurements produced in native full-resolution are often referred to as "single-look" measurements. In contrast, "multi-looked" measurements are acquired by averaging the complex returns of adjacent pixels. InSAR time-series methods can be categorized into two groups: Persistent scatterers interferometry (PSI) and distributed scatterers interferometry (DSI). PSI makes use of high signal-to-noise ratio *single-look* measurements and only requires $N-1$ common-scene interferograms formed from N SAR images [13], [14]. In contrast, DSI identifies partially correlated areas and may use *multi-looking* to reduce stochastic noise and to improve phase estimation [15]. DSI can be further divided into two categories. One estimates phase time-series by solving a linear system of unwrapped interferometric phases, e.g., the conventional Small BAseline Subset (SBAS) technique [16]. The other category exploits the SAR correlation matrix and retrieves a phase history before phase unwrapping [17]–[19], e.g., SqueeSAR [19].

Comparisons between the two families of time-series methods reveal systematic differences in estimated line-of-sight (LOS) deformation maps [20], [21], which were initially considered to be within expected noise levels [20]. However, [22] finds that the discrepancies increase with decreasing temporal baseline imposed on the DSI method. This observed correlation with the temporal baseline cannot be explained by known noise terms and therefore indicates the presence of a previously overlooked phase component introduced by multi-look processing. The observations of non-zero closure phase [23], which result from an inconsistency among a triplet of multi-looked interferometric phases formed from three acquisitions, also corroborate the existence of a such phase component. However, the cause of closure phase remains unclear with previous studies differing on whether to relate closure phase to a physical process such as soil moisture change [23], pure statistical properties of SAR measurements [24] or a combination of these factors. Understanding the cause of closure phase and its impact on the performance of DSI time-series algorithms is therefore crucial for determining the error budget and optimal processing approach as well as accurate interpretations of ground displacement time-series derived from InSAR measurements.

The purpose of this work is to investigate the cause of both non-zero closure phase and the observed discrepancies between DSI and PSI time-series. Specifically, we highlight the roles of multi-look processing and inhomogeneity within a multi-look window. In the context of deformation studies, these discrepancies can *bias* interpretations of InSAR-derived displacement time-series. In this paper, we refer to these discrepancies as *bias* although they are results of physical processes such as moisture change. In Section II of this paper, we review concepts of closure phase, multi-look processing

Y. Zheng and M. Simons are with the Division of Geological and Planetary Science, California Institute of Technology.

H. Fattahi and P. Rosen are with the Jet Propulsion Laboratory, California Institute of Technology.

P.Agram is with Descartes Labs.

and InSAR time-series analysis. In Section III, we demonstrate our model for multi-looked interferometric phase that can explain both non-zero closure phase and observed discrepancies in DSI and PSI time-series. In Section IV, we introduce the method for estimating bias time-series using generalized closure phase measurements. We show simulation results in Section V and the workflow of our approach in Section VI. We then validate our model with a case study in Barstow-Bristol Trough, California in Section VII. We discuss closure phase and systematic biases in multi-looked SAR interferometry in Section VIII. We conclude in Section IX.

II. Technical Background

A. Closure Phase Definition

With three SAR Single Look Complex (SLC) images s_i, s_j, s_k, where i, j, k are acquisition indices, three interferograms can be generated z_{ij}, z_{jk}, z_{ki}. Closure phase is defined as the angle of the triple product of the aforementioned three interferometric measurements:

$$\Delta\phi_{ijk} = \angle z_{ij} z_{jk} z_{ki} \tag{1}$$

which is also the sum of the three respective interferometric phases (modulo 2π)

$$\Delta\phi_{ijk} = \Delta\phi_{ij} + \Delta\phi_{jk} + \Delta\phi_{ki}. \tag{2}$$

Single-look interferometric phase can be decomposed as the difference between SAR phases at two acquisition times $\Delta\phi_{ij} = \phi_i - \phi_j$, where ϕ_i represents the SAR phase at time t_i. Therefore for single-look interferograms, it is straightforward to derive $\Delta\phi_{ijk} \equiv 0$. Closure phase has also been referred to in literature as "phase consistency" [23] or "phase triangularity" [19]. In contrast to the single-look case, closure phases are generally nonzero for multi-looked observations [23], [25], [26]. We consider pixels with zero closure phase as pixels with "consistent" phase measurements and pixels with nonzero closure phase as pixels with "inconsistent" phase measurements.

B. Multi-look Processing

Multi-look processing is an effective way to reduce phase noise over DS pixels in InSAR observations [27].

An L-look interferometric measurement is generated by averaging L single-look measurements. Assuming that these L measurements are independent and statistically homogeneous, i.e., they are drawn from the same Probability Density Function (PDF), the L-look measurement z is the Maximum Likelihood (ML) estimate and is unbiased [15]:

$$E(z) = \rho\sigma e^{i\Delta\phi} \tag{3}$$

where ρ is the coherence magnitude between the two SAR observations, σ is a measure of the average power of the two SAR images, and $\Delta\phi$ is the true interferometric phase. $E(\cdot)$ represents the expectation of a random variable. The ML estimate of the interferometric phase is biased [15] unless the interferogram is properly unwrapped [28]. In this work, we assume that the deviation is negligible: $E(\angle z) \approx \angle E(z) = \Delta\phi$.

C. Phase closure is an intrinsic assumption in InSAR time-series

DSI methods operate on multi-looked InSAR measurements and assume phase consistency for multi-looked phase, i.e.,

$$\Delta\phi_{ij} = \phi_i - \phi_j + \Delta\phi^n \tag{4}$$

where ϕ_i represents the SAR phase at time t_i and $\Delta\phi^n$ is a zero-mean noise component. With this assumption , one can derive that closure phase is expected to be zero.

$$E(\Delta\phi_{ijk}) = 0 \tag{5}$$

However, non-zero closure phase has been widely observed [23], [25], indicating the presence of a previously overlooked phase component introduced by multi-look processing that breaks the assumption of phase consistency and introduces bias in InSAR time-series.

III. Multi-look processing inhomogeneous interferometric measurements

We represent inhomogeneity with two groups of measurements with distinct Probability Density Functions (PDFs). Though it is possible to describe inhomogeneity with a continuous distribution such as the work presented in [29], we find a simple dyad model sufficient to provide useful insights. Consider two groups of pixels inside one multi-look window. The true phase of each group is represented by $\Delta\phi^{\mathrm{I}}$ and $\Delta\phi^{\mathrm{II}}$. Multi-look processing leads to the following expected measurement:

$$E(z) = (1-q)\rho^{\mathrm{I}}\sigma^{\mathrm{I}} e^{j\Delta\phi^{\mathrm{I}}} + q\rho^{\mathrm{II}}\sigma^{\mathrm{II}} e^{j\Delta\phi^{\mathrm{II}}} \tag{6}$$

where q is the percentage of pixels in group II with respect to the total number of pixels in the multi-look window. Let w be the weight of the amplitude of group II comparing to the sum of amplitudes of both groups.

$$w = \frac{q\rho^{\mathrm{II}}\sigma^{\mathrm{II}}}{q\rho^{\mathrm{II}}\sigma^{\mathrm{II}} + (1-q)\rho^{\mathrm{I}}\sigma^{\mathrm{I}}} \tag{7}$$

The expected multi-looked phase is a function of $\Delta\phi^{\mathrm{I}}$, $\Delta\phi^{\mathrm{II}}$, and w.

$$E(\Delta\phi) = \angle\{(1-w)e^{j\Delta\phi^{\mathrm{I}}} + we^{j\Delta\phi^{\mathrm{II}}}\} \tag{8}$$

When $w \to 0$, $E(\Delta\phi) = \Delta\phi^{\mathrm{I}}$. When $w \to 1$, $E(\Delta\phi) = \Delta\phi^{\mathrm{II}}$. Both $w \to 0$ and $w \to 1$ represent cases where one group of measurements is dominant so that inhomogeneity is negligible. When $|\Delta\phi^{\mathrm{I}} - \Delta\phi^{\mathrm{II}}| < 1$ radian, $E(\Delta\phi)$ can be approximated as a linear function of $\Delta\phi^{\mathrm{I}}$ and $\Delta\phi^{\mathrm{II}}$ (Appendix A):

$$E(\Delta\phi) \approx (1-w)\Delta\phi^{\mathrm{I}} + w\Delta\phi^{\mathrm{II}} \tag{9}$$

Therefore, the multi-looked phase carries information from both $\Delta\phi^{\mathrm{I}}$ and $\Delta\phi^{\mathrm{II}}$. Eq. (9) can be extended to multiple groups with the contribution from each group weighted by their respective amplitude ratio.

Generally the interferometric phase of repeat pass interferograms consists of different components such as propagation

delay, geometrical phase induced by baseline separation between orbits, motion of the ground surface, and decorrelation noise. For the sake of simplicity, we assume that a multi-look window consists of two groups of pixels such that both groups are subjected to ground deformation ($\Delta\phi^{\text{def}}$) while one group also undergoes an additional process ($\Delta\phi^{\text{x}}$),

$$\begin{aligned}\Delta\phi^{\text{I}} &= \Delta\phi^{\text{def}} \\ \Delta\phi^{\text{II}} &= \Delta\phi^{\text{def}} + \Delta\phi^{\text{x}}\end{aligned} \tag{10}$$

This simplification does not affect our formulation in the following as one could substitute deformation with a sum of all interferometric phase components which results in consistent phase (i.e., zero closure phase). Hereinafter, we refer to processes that result in zero closure phase *temporally consistent processes* and processes that result in nonzero closure phase *temporally inconsistent processes*. With this assumption,

$$E(\Delta\phi) = \Delta\phi^{\text{def}} + w\Delta\phi^{\text{x}} \tag{11}$$

and the expected closure phase is therefore:

$$\begin{aligned}E(\Delta\phi_{ijk}) = w_{ij}(\phi_i^{\text{x}} - \phi_j^{\text{x}}) + w_{jk}(\phi_j^{\text{x}} - \phi_k^{\text{x}}) \\ - w_{ik}(\phi_i^{\text{x}} - \phi_k^{\text{x}})\end{aligned} \tag{12}$$

$E(\Delta\phi_{ijk}) \neq 0$ except in the following cases:

1) $\phi_i^{\text{x}} = \phi_j^{\text{x}} = \phi_k^{\text{x}}$. This is a trivial situation where $E(\Delta\phi^{\text{x}}) = 0$ in all three interferograms. For example, decorrelation caused by random movements of scatterers does not induce systematic phase change and hence does not result in non-closure.

2) $w_{ij} = w_{jk} = w_{ik}$. In other words, the weight w for the time-inconsistent process remains a constant in all three interferograms. For example, processes such as deformation or atmospheric delays do not induce amplitude or correlation change and hence do not result in non-closure.

Therefore non-zero closure phase signals the presence of phase-changing physical processes with varying weights of amplitudes in different interferograms. The weight w_{ij} (Eq.(7)) is a function of both time t_i and t_j. We can simplify w_{ij} as a function of the temporal baseline $\Delta t = |t_i - t_j|$ if (1) q is a function of Δt, i.e., the number of pixels that undergo the temporally inconsistent process changes with the temporal span and/or (2) $\rho^{\text{II}}/\rho^{\text{I}}$ is a function of Δt. Both of these conditions effectively vary the amplitude representation of the temporally inconsistent process within the multi-look window as a function of the temporal span Δt. These conditions can be satisfied by a single process or a combination of processes that induce both amplitude and phase change for a subset of pixels within the multi-look window.

It is worth noting that although we started this derivation with multi-looking inhomogeneous interferometric measurements, spatial inhomogeneity is not a required condition for causing non-closure. For example, if $w_{ij} = 0, w_{jk} = w_{ik} = 1$, hence inhomogeneity is negligible in all three interferograms, $E(\Delta\phi_{ijk}) = \phi_j^{\text{x}} - \phi_i^{\text{x}}$. As long as $\phi_i^{\text{x}} \neq \phi_j^{\text{x}}$, $E(\Delta\phi_{ijk}) \neq 0$.

IV. Modeling systematic bias in InSAR time-series

If the weight w of the temporally inconsistent process varies with the temporal baseline, the derived time-series vary with the temporal baseline as well. For example, if $w(\Delta t < 30 \text{ days}) = 0.5$ and $w(\Delta t > 30 \text{ days}) = 0$, using a subset of interferograms with a temporal baseline smaller than 30 days will result in the following phase time-series:

$$\phi_i = \phi_i^{\text{def}} + 0.5\phi_i^{\text{x}}. \tag{13}$$

In contrast, if only using interferograms with temporal baseline longer than 30 days, then

$$\phi_i = \phi_i^{\text{def}}. \tag{14}$$

Time-series analysis with 30 days temporal baseline therefore contains a *bias* which reflects contributions from the temporally inconsistent process. In this section, we present a model that predicts the contribution from temporally inconsistent processes in the derived time-series.

Assume that we have N consecutive radar measurements acquired every δ_t days. We define a connection-n (con-n) interferometric pair as SAR acquisitions separated by n acquisition intervals. We refer to analysis of interferograms comprised of con-1 through con-n pairs as a bandwidth-n (bw-n) analysis. The system of equation for a bw-n analysis is:

$$\boldsymbol{\Delta\phi} = A\boldsymbol{\phi}^{\text{def}} + WA\boldsymbol{\phi}^{\text{x}} \tag{15}$$

where $\boldsymbol{\Delta\phi}$ is a $M \times 1$ ($M = n(2N-n-1)/2$) interferometric phase vector, A is a $M \times N$ design matrix specifying SAR acquisitions used, $\boldsymbol{\phi}^{\text{def}}$ and $\boldsymbol{\phi}^{\text{x}}$ represent phase histories of deformation and the temporally inconsistent process, respectively, and W is a $M \times M$ diagonal matrix indicating the weight of the temporally inconsistent process in each interferometric pair.

$$W_{ii} = w(k_i\delta_t) \tag{16}$$

where $i = 1, 2, ...M$ and k_i is the connection level of the interferometric pair specified in the i^{th} row of A. InSAR time-series algorithms do not distinguish between $\boldsymbol{\phi}^{\text{def}}$ and $\boldsymbol{\phi}^{\text{x}}$ and solve the following system of equation

$$\boldsymbol{\Delta\phi} = A\boldsymbol{\phi}. \tag{17}$$

Combining Eqs.(15) and (17),

$$A\boldsymbol{\phi} = A\boldsymbol{\phi}^{\text{def}} + WA\boldsymbol{\phi}^{\text{x}} \tag{18}$$

The reconstructed phase history $\boldsymbol{\phi}$ from a bw-n analysis is therefore a combination of both deformation and the temporally inconsistent process.

$$\boldsymbol{\phi} = \boldsymbol{\phi}^{\text{def}} + A^{\dagger}WA\boldsymbol{\phi}^{\text{x}} \tag{19}$$

The bias time-series is thus

$$\boldsymbol{\phi}^{\text{bias}} = A^{\dagger}WA\boldsymbol{\phi}^{\text{x}} = A^{\dagger}W^{r}Aw(\delta_t)\boldsymbol{\phi}^{\text{x}} \tag{20}$$

where W^r is a $M \times M$ diagonal matrix with diagonal component $W_{ii}^r = W_{ii}/w(\delta_t)$, $i = 1, 2, ..., M$.

We exploit sequential closure phases to estimate W^r and $w(\delta_t)\phi^{\mathrm{x}}$. We define a con-$n$ sequential closure phase starting at acquisition i as

$$\Phi_i^n = \Big(\sum_{k=i}^{i+n-1} \phi_{k,k+1}\Big) - \phi_{i,i+n} \tag{21}$$

$$= \big(w(\delta_t) - w(n\delta_t)\big)(\phi_{i+n}^{\mathrm{x}} - \phi_i^{\mathrm{x}}) \tag{22}$$

We use sequential closure phases because (1) sequential closure phases describe the phase difference of the temporally inconsistent process between n acquisitions, and (2) sequential closure phases are sensitive to the weights of the temporally inconsistent process.

Sequential closure phases can be used to infer weighted phase history of the temporally inconsistent process. For example, with $\phi_1^{\mathrm{x}} = 0$

$$\begin{aligned} \Phi_1^n &= \big(w(\delta_t) - w(n\delta_t)\big)\phi_{1+n}^{\mathrm{x}} \\ \Phi_1^n + \Phi_{1+n}^n &= \big(w(\delta_t) - w(n\delta_t)\big)\phi_{1+2n}^{\mathrm{x}} \\ \Phi_1^n + \Phi_{1+n}^n + \Phi_{1+2n}^n &= \big(w(\delta_t) - w(n\delta_t)\big)\phi_{1+3n}^{\mathrm{x}} \\ \dots \quad &\dots \end{aligned} \tag{23}$$

Thus, we can construct a weighted phase history f_k^n, $k = 1, ..., N$, of the temporally inconsistent process by summing consecutive sequential closure phases. The superscript n indicates the connection level of sequential closure phases and determines the weights imposed on the phase history

$$f_k^n = n\big(w(\delta_t) - w(n\delta_t)\big)\phi_k^{\mathrm{x}} \qquad n \geq 2 \tag{24}$$

where

$$f_k^n = \begin{cases} 0 & k = 1 \\ \sum_{i=1}^{k-1} \Phi_i^n & 1 < k \leq N - n \\ (k - N + n)\Phi_{N-n}^n + \sum_{i=1}^{N-n-1} \Phi_i^n & k > N - n \end{cases} \tag{25}$$

Note that since each con-n sequential closure phase describes the phase difference between n time steps, the estimated bias time-series has a temporal resolution of $n\delta_t$.

A. Estimate $w(\delta_t)\phi^x$

Since the observed discrepancies between DSI and PSI time-series decrease with the temporal baseline, we make the assumption that the weight of the temporally inconsistent process decreases monotonically with increasing time span, and the weight becomes negligible when the time span becomes equal or larger than $n_l\delta_t$, i.e.,

$$\frac{w(n\delta_t)}{w(\delta_t)} = 0, n \geq n_l. \tag{26}$$

Let $n = n_l$ in Eq. (24),

$$f_k^{n_l} = n_l w(\delta_t)\phi_k^{\mathrm{x}} \tag{27}$$

Therefore by summing con-n_l sequential closure phases at different starting acquisition i, we can obtain an estimate for $w(\delta_t)\phi^{\mathrm{x}}$

$$w(\delta_t)\phi_k^{\mathrm{x}} = \frac{f_k^{n_l}}{n_l}, \qquad k = 1, 2, ..., N \tag{28}$$

B. Estimate W_r

Combining Eqs. (24) and (28) and let $k = N$

$$\frac{w(n\delta_t)}{w(\delta_t)} = 1 - \frac{f_N^n/n}{f_N^{n_l}/n_l} \qquad n \geq 2 \tag{29}$$

This equation allows us to populate the matrix W_r in Eq. (20).

With the estimate of both $w(\delta_t)\boldsymbol{\phi}^{\mathrm{x}}$ and W_r, along with the design matrix A, we can reconstruct the bias time-series ϕ^{bias} using Eq. (20). The temporal resolution of the reconstructed bias time-series is $n_l\delta_t$. To achieve finer temporal resolutions, we can substitute con-n_l sequential closure phases with con-m ($2 \leq m < n_l$) sequential closure phases by combining Eqs. (24) and (29):

$$\frac{f_k^{n_l}}{n_l} = \frac{f_N^{n_l}/n_l}{f_N^m/m}\frac{f_k^m}{m} \tag{30}$$

V. Simulation

We simulate a multi-look window that deforms periodically while half of the pixels also go through a temporally inconsistent process. We assume that the temporally inconsistent process can be described by an inherent physical parameter that linearly increases with time $x_i = 0.025\frac{t_i}{\delta_t}$ where δ_t is the acquisition interval. The parameters of the multi-look window are described in Table. I

TABLE I
PARAMETERS OF THE MULTI-LOOK WINDOW

	Group I (deformation)	Group II (deformation + temporally inconsistent process)
$\Delta\phi_{ij}$	$\Delta\phi_{ij}^{\mathrm{def}}$	$\Delta\phi_{ij}^{\mathrm{def}} + \frac{2}{3}\pi(x_j - x_i)$
ρ_{ij}	1	$e^{-4\lvert x_i - x_j\rvert}$
σ	1	1

The multi-looked interferometric phase between the i^{th} and j^{th} acquisitions is therefore (Eq. (6)),

$$\Delta\phi_{ij} = \angle\{\frac{1}{2}e^{j\Delta\phi_{ij}^{\mathrm{def}}} + \frac{1}{2}e^{-4|x_i - x_j|}e^{j(\Delta\phi_{ij}^{\mathrm{def}} + \frac{2}{3}\pi(x_j - x_i))}\} \tag{31}$$

The simulated phase histories of the temporally inconsistent process and deformation are shown as the dashed line and the solid line in Fig. 1, respectively. We perform bw-1, bw-5, bw-10 and full bandwidth analysis. The reconstructed time-series are weighted averages of both deformation and the temporally inconsistent process (Fig. 1(a)). With the primary goal of recovering deformation, the temporally inconsistent process constitutes as *bias* in the reconstructed time-series.

Fig.1 (b) and (c) show the corrected time-series with $n_l = 15$ and $n_l = 30$, respectively. In both cases, the amount of biases are significantly reduced. Note that the corrected time-series with $n_l = 30$ contain less bias than the time-series obtained from a full-network analysis. Since the choice of n_l in either case is imperfect (Fig. 2), the estimation of the weight matrix W_r is not perfect and hence the biases are not completely eliminated.

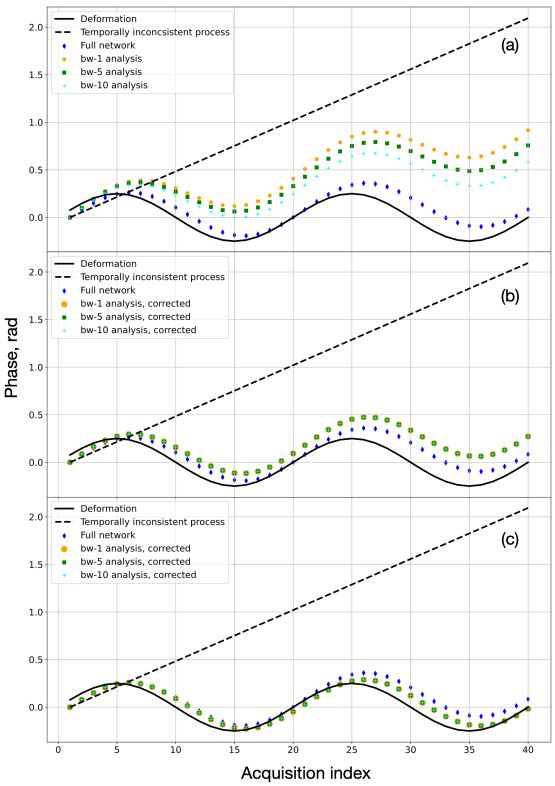

Fig. 1. Time-series of bw-1 (orange circle), bw-5 (green square), bw-10 (cyan plus), and full bandwidth (blue diamond) analysis (a) before correction, (b) after correction with $n_l = 15$ and (c) after correction with $n_l = 30$. The solid line shows the simulated phase history of deformation. The dashed line shows the simulated phase history of the temporally inconsistent process.

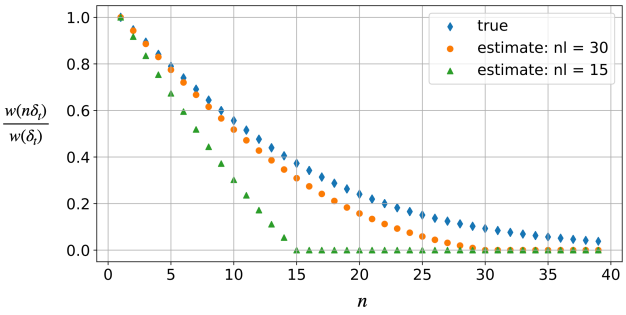

Fig. 2. The true values of $w(n\delta_t)/w(\delta_t)$ (blue circles) and the estimated values of $w(n\delta_t)/w(\delta_t)$ with the assumptions of $n_l = 15$ (green triangle) and $n_l = 30$ (orange squares).

VI. Bias Estimation Algorithm

To estimate the *bias* in a bw-n time-series, we first need to determine n_l so that $w(n_l\delta_t)/w(\delta_t) \rightarrow 0$ (Eq.(26)). In practice, without prior knowledge of the temporally inconsistent process, the choice of n_l is empirical and constrained by the total number of acquisitions ($n_l < N$).

It is often useful to have a proxy map that identifies bias-susceptible regions. We can do so by evaluating $\tau = \frac{1}{K}\sum_{k=1}^{K} e^{j\Phi_k^{n_l}}$. The amplitude of τ ranges between 0 and 1 and is dominated by decorrelation effects [30], [31]. The phase of τ describes the average phase change of the temporally inconsistent process per acquisition. Consider two end-member cases: (1) If a multi-looked measurement is fully decorrelated, then $|\tau| \rightarrow 0$, $\angle\tau$ varies between $-\pi$ to π with an approximate Gaussian distribution (central limit theorem); (2) If a multi-looked measurement has minimal temporal decorrelation, then $|\tau| \rightarrow 1$, $\angle\tau$ is the average phase change of the temporally inconsistent process per acquisition. Thus, by setting a threshold on both the amplitude and the phase of τ, i.e., $|\tau| > \epsilon$ and $|\angle\tau| > \theta$, we can obtain a proxy map that identifies regions susceptible to bias.

The next step is to form con-n_l sequential closure phases $\Phi_1^{n_l}, ..., \Phi_{N-n_l}^{n_l}$ defined in Eq. (21). We first form wrapped sequential closure phase from either a coregistered stack of single-look complex (SLC) SAR images or a redundant network of existing interferograms. We use wrapped closure phases to reduce the impact of potential phase unwrapping errors in interferograms. We next unwrap sequential closure phases and reconstruct the weighted phase history $f_1^{n_l}, ..., f_N^{n_l}$ of the temporally inconsistent process by summing the sequential closure phases (Eq. (25)). The *bias* time-series of the bw-1 analysis $w(\delta_t)\phi^z$ is therefore $[f_1^{n_l}/n_l, ..., f_N^{n_l}/n_l]$.

We then form sequential closure phases from con-2 to con-n and their respective weighted temporally inconsistent phase histories $(f_k^2, ..., f_k^n, k = 1, ..., N)$ in order to populate the matrix of W^r. The accuracy of the matrix W^r is determined by the estimation accuracy of $w(n\delta_t)/w(\delta_t)$.

Finally we solve the linear equation defined in Eq.(20).

The summary of the above algorithm is illustrated in Fig.3.

VII. Validation with Data

We processed 153 Sentinel 1 A/B SAR images (descending path 173) using ISCE2 (https://github.com/isce-framework/isce2) from February 2017 to January 2021 of the Barstow-Bristol trough area, California, USA (Fig. 4). The test site is characterized by desert landscapes and have several dry lakes as a result of arid climate [32]–[34]. We form 1475 interferograms (con-1 through con-10) and multi-look each interferogram by 10 looks in the azimuth direction and 40 looks in the range direction. We unwrap the interferograms using the SNAPHU algorithm [35].

Following the workflow presented in Fig. 3, we first create a proxy map that highlights regions susceptible to bias by evaluating the parameter $\tau = \frac{1}{K}\sum_{k=1}^{K} e^{j\Phi_k^{n_l}}$ (Fig. 5). We assume $n_l = 20$. We choose an amplitude threshold $|\tau|$ of 0.3 to remove rapidly decorrelating areas and a phase threshold of 0.3 radian to select areas with systematic non-zero closure phase. The phase threshold is determined as the 2σ value of a Gaussian distribution with $\sigma = \frac{\pi}{\sqrt{3K}}$. The proxy map provides a quick view of possible bias regions. We then perform time-series analysis of bw-1, bw-5 and bw-10

This article has been accepted for publication in a future issue of this journal, but has not been fully edited. Content may change prior to final publication. Citation information: DOI 10.1109/TGRS.2022.3167648, IEEE Transactions on Geoscience and Remote Sensing

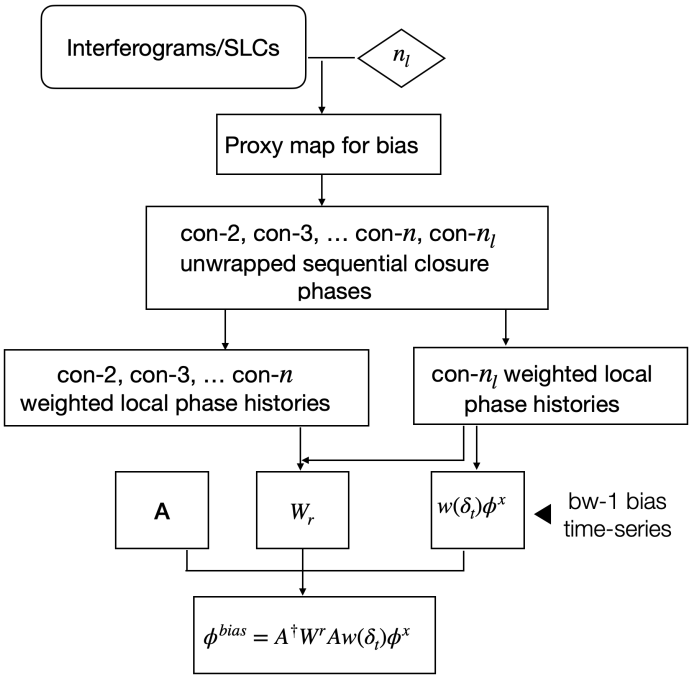

Fig. 3. Workflow of reconstructing the bias time-series in a bw-n time-series analysis.

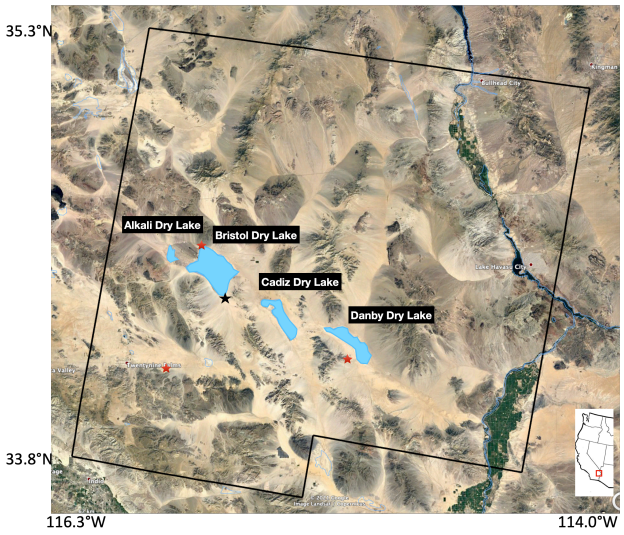

Fig. 4. Google Earth map of the test site (black lines) in Barstow-Bristol trough, California, USA. Locations of the dry lakes are marked with blue patches. From left to right, Alkali dry lake, Bristol dry lake, Cadiz dry lake and Danby dry lake. Red stars indicate the locations of the weather stations used in this study.

using MintPy [36]. Fig. 6 (top row) presents the estimated displacement velocity maps. The average velocity map derived from bw-1 analysis (top row, left) shows that the dry lakes and their surrounding areas are characterized by signals that appear to move towards the satellite. The uplift of the dry lake beds has been observed in other regions [37] and may be related to formation of evaporite mineral crystals [38]. While the apparent uplift of the dry lakes remains consistent in all three velocity maps, the signals of their surrounding areas fade rapidly in the longer-connection velocity maps. Note

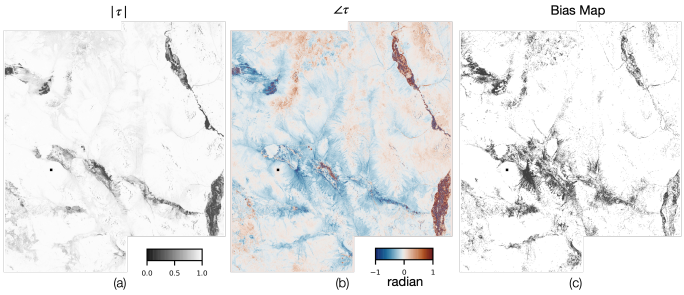

Fig. 5. Maps identifying bias regions by evaluating $\tau = \frac{1}{K}\sum_{k=1}^{K} e^{j\Phi_k^{n_l}}$ (a) $|\tau|$ and (b) $\angle\tau$ (c) Bias map by using the thresholds of $|\tau| > 0.3$ and $|\angle\tau| > 0.3$ radian. Black pixels are identified as regions susceptible to bias.

that these areas with velocity discrepancies are also identified in the bias map (Fig.5(c)).

We then estimate the bias velocity in a bw-1 analysis. We find strong bias presences surrounding the dry lakes – reaching 1 cm/year in areas near the Bristol dry lake (the color scale in Fig.7 is saturated for better visual effects). Other notable areas with bias include the back side of mountains with respect to the radar view and areas surrounding the agricultural region along the Colorado river. While the bias surrounding the dry lakes are positive (range decrease relative to the reference pixel), the bias in the other areas are negative (range increase with respect to the reference pixel). We proceed to estimate the elements of W_r and compute maps of $w(2\delta_t)/w(\delta_t)$, $w(3\delta_t)/w(\delta_t)$ and $w(5\delta_t)/w(\delta_t)$. By multiplying these weight ratio maps with the bw-1 bias velocity, we acquire bias velocities in con-2, con-3, and con-5 interferograms (Fig. 7 (b)-(d)). We find that the bias velocity drops rapidly with increasing temporal baseline. In con-5 interferograms which have an average temporal baseline of 45 days, the bias velocity drops to below 2 mm/year in nearly all areas.

Finally we estimate *bias* time-series associated with temporally inconsistent processes in each velocity map (Fig. 6, middle row). The corrected velocity maps (Fig. 6, bottom row) show consistent patterns. In comparison, the full-bandwidth result obtained with the Fringe package [39] shows no apparent uplift signal surrounding the dry lake, consistent with the corrected velocity maps (Fig. 8).

It is worth noting that since phase unwrapping is performed in both regular time-series analysis and in the bias estimation, phase unwrapping errors may impact both the estimated original and bias time-series. We use the connected component information produced by phase unwrapping algorithms such as SNAPHU [35] to mask out areas that may have phase unwrapping errors. We retain areas that are within the same connected component in all unwrapped sequential closure phases and velocity solutions and mask out all other areas. In this case, most regions of the test site are deemed reliably unwrapped except for agricultural fields and some areas within the dry lakes (Fig. 6).

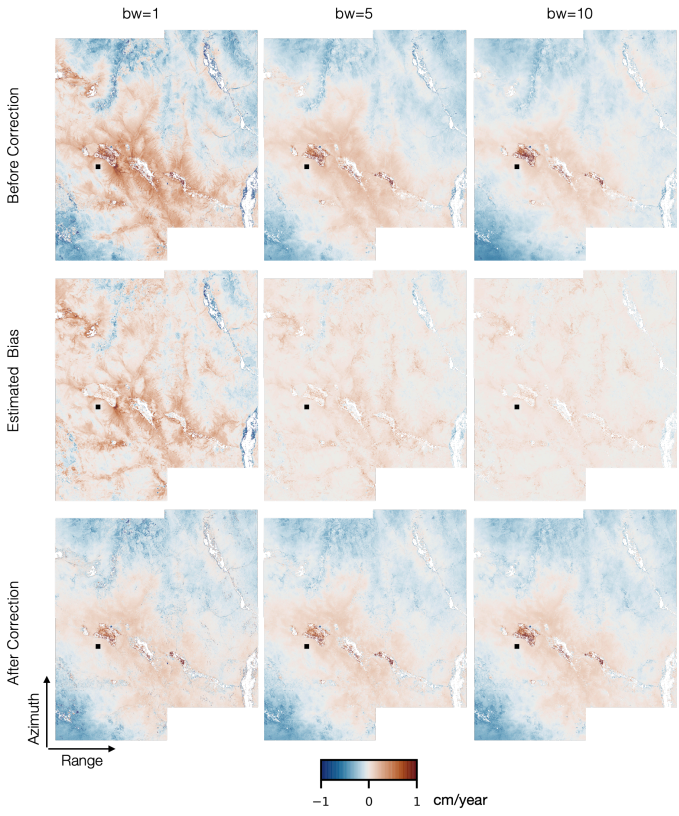

Fig. 6. Displacement velocity maps in the radar coordinate derived from time-series of (left column) bw-1 analysis, (middle column) bw-5 analysis, and (right column) bw-10 analysis. After removing the estimated signals associated with temporally inconsistent processes (middle row) from original velocities maps (top row), the residual velocity maps (bottom row) are consistent. Areas with phase unwrapping errors are masked out. The reference point is marked by a black square.

VIII. Discussion

A. Choice of n_l

The first step of our workflow is to determine n_l. In theory, we should choose a value of n_l so that con-n_l interferograms are free of bias. In practice, we have to choose n_l empirically unless we have some prior knowledge of the temporally inconsistent processes. The number of total acquisitions also limits the choice of n_l. We cannot simply choose the largest possible value for n_l (e.g., $n_l = N$) because long connection sequential closure phases are more likely to suffer from temporal decorrelation and therefore are difficult to unwrap. In our case, we choose $n_l = 20$ while we have $N = 153$ acquisitions. We have shown in Section V that imperfect choice of n_l results in partial bias correction. More accurate choices of n_l yield more accurate bias correction.

We can validate the choice of n_l by examining decay rates of bias velocities. The chosen value for n_l is reasonable if the derived bias velocities become negligible at a temporal baseline much smaller than $n_l\delta_t$. In our case, since con-5 interferograms contain less than 2 mm/year bias velocity, our choice of $n_l = 20$ at least reduces bias to below 2 mm/year.

B. Phase Unwrapping Errors

Since our algorithm requires unwrapping sequential closure phases, it is subjected to phase unwrapping errors. Phase unwrapping errors are strongly associated with regions with high decorrelation noise. To reduce the impact of phase unwrapping errors, one can mask out areas that may suffer from phase unwrapping errors. In our test case, we mask out areas with phase unwrapping errors using connected component information from SNAPHU. Other ways to mask out or correct for phase unwrapping errors include utilizing unwrapped closure phases and accounting for the multiples of 2π residue [36], [40]. In rapidly decorrelating regions, such a mask may not be practical even with a choice of small n_l. In this case, bias correction may not be possible and we recommend producing an indication map identifying regions of potential bias such as Fig.5(c). If the primary goal is to recover deformation, such a map can mask out areas that are impacted by biases.

C. The assumptions for the weight w_{ij}

In our algorithm, we make two assumptions about the weight w_{ij}.

First, we simplify the weight w_{ij} to be a function of a single parameter $w_{ij} = w(|t_i - t_j|)$ rather than two parameters $w_{ij} = w(t_i, t_j)$. We make this simplification based on the observed correlation between temporal baseline and the discrepancy between PSI and DSI time-series. This simplification also allows us to perform bias estimation with a small sets of parameters. In reality, this assumption may not capture the complexity of real processes. We find that as long as w_{ij} can be approximated as a function of the temporal baseline, the proposed algorithm works well (Appendix B).

The second assumption is that w_{ij} fades over time. We make this assumption based on observations that DSI time-series with short temporal baseline show larger discrepancies with PSI time-series. To account for scenarios that this assumption is not met, we need to develop more advanced algorithms building on our model for multi-looked phase (Eq.(9)).

D. Does small-baseline analysis always contains bias?

Though [22] recommends the use of a full-network to eliminate bias, we find that full-network approach is not always necessary. For example, in our case study, the bw-10 analysis contains negligible bias (Fig. 6) because the decay rate of the bias-inducing process is rapid (Fig. 7). On the other hand, if the decay rate for the bias-inducing process is slow relative to the length of observation, even a full-network approach does not completely eliminate the bias (Fig. 1).

E. Alternative Time-series methods

Depending on the decay rate of the bias-inducing process, alternative time-series methods [30], [41], [42] may also produce results that show no discrepancies among DSI time-series with different temporal baselines. This is because the

This article has been accepted for publication in a future issue of this journal, but has not been fully edited. Content may change prior to final publication. Citation information: DOI 10.1109/TGRS.2022.3167648, IEEE Transactions on Geoscience and Remote Sensing

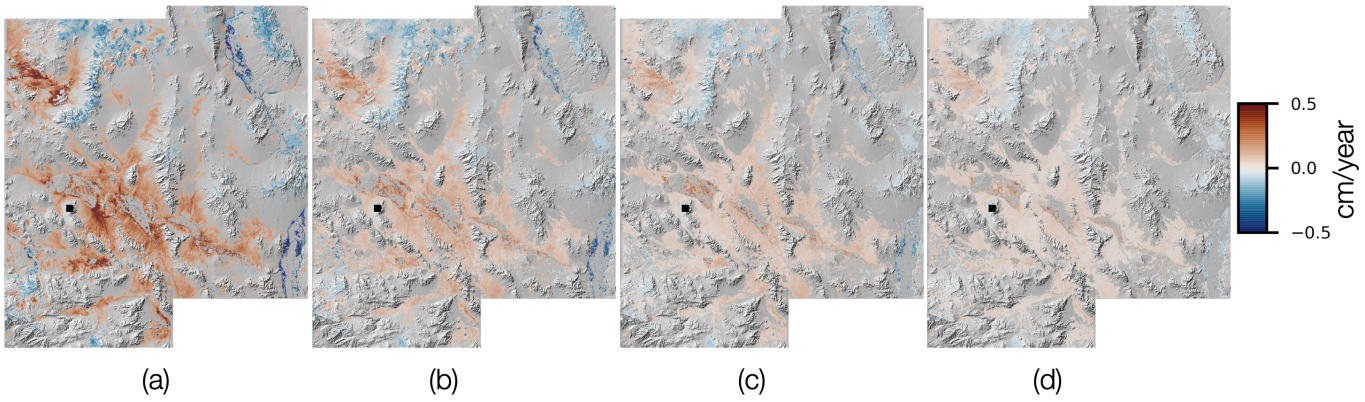

Fig. 7. Maps of bias velocities in (a) con-1, (b) con-2, (c) con-3, and (d) con-5 interferograms. The average temporal baselines are (a) 9 days, (b) 19 days, (c) 28 days, and (d) 45 days overlain on shaded relief topography maps. The color bar is saturated in (a) for better visual effects. Areas with absolute bias velocity smaller than 1 mm/year in (a) are masked. All velocities are relative to a reference pixel represented by a black square on the plots.

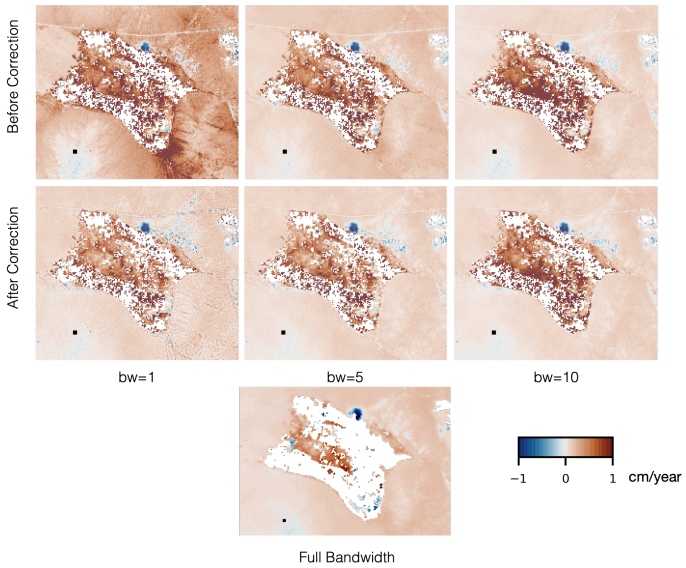

Fig. 8. (top) Original and (middle) corrected displacement velocity maps in the radar coordinate over the Bristol Dry lake region (marked in Fig.4) derived from (left) bw-1, (middle) bw-5 and (right) bw-10 analysis. The corrected velocity maps do not show the apparent uplift signal in the region around the dry lake, consistent with the (bottom) displacement velocity map derived from full-bandwidth analysis. Areas with phase unwrapping errors are masked out.

triangulation step or an equivalent preprocessing noise filtering step implemented in these work eliminates inconsistent phase component in interferograms before time-series inversion. However, removal of inconsistent phase component is not equivalent to removal of bias. Consider a simple case where the weight for the bias-inducing process remains a constant. Since no inconsistent phase arises from the bias-inducing process, no bias is removed from triangulation. Rather than filtering out inconsistent phase before inversion, our method predicts the contribution from the bias-inducing process in the time-series. The main difference between the proposed algorithm with these algorithms is that our method models the temporal characteristics of the bias-inducing process while the noise-filtering triangulation considers the bias-inducing process as white noise.

F. Nature of temporally inconsistent processes

While we identify temporally inconsistent processes that have varying representation inside a multi-look window the root cause for non-zero closure phase and bias in DSI time-series, the nature of these temporally inconsistent processes remains undetermined. Soil moisture and vegetation has been suggested as two possible causes for the observed bias in the time-series [22], [23]. We examine one pixel that exhibits significant bias on the edge of the Bristol dry lake (marked in Fig. 4 as a black star). We acquire precipitation data from three near by stations (marked as red stars in Fig.4) from the National Centers for Environmental Information (NCEI) and compare cumulative precipitation with the estimated bias time-series. The correlation between the bias time-series and cumulative precipitation (Fig. 9, top) suggests that the temporally inconsistent process may reflect the drying process in the soil after precipitation. Perhaps unintuitively, precipitation does not result in a phase jump, but rather the onset of gradual phase decrease (motion towards the satellite) over a period of a few weeks or months. The lack of instant phase jumps may be due to the inherent relative nature of InSAR phase measurements with respect to a reference point. We form two coherence time-series, one with a dry reference date (Nov 10th, 2014) and the other with a wet reference date (Feb 3rd, 2017). This particular pixel suffers from little temporal decorrelation and its correlation time-series show clear impacts from precipitation events. In particular, we observe instant correlation loss and gradual recovery in response to precipitation in the dry correlation time-series (gray triangles, red line). The recovery time of the correlation matches the duration of phase changes after a precipitation event. The wet correlation time-series (black pluses, blue line) mirrors the dry correlation time-series, with opposite response to precipitation. Similar InSAR correlation response to precipitation events has been reported by [43]. The derived bias time-series likely reflect the InSAR phase

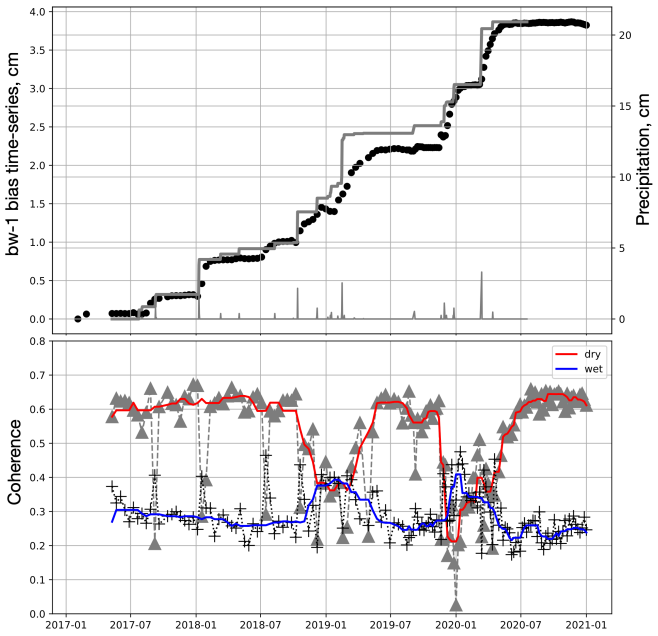

Fig. 9. (Top) The bw-1 bias (black) time-series of a point at the rim of the Bristol dry lake (marked as a black star in Fig.4) plotted against cumulative precipitation data (gray) averaged over three nearby stations (marked as red stars in Fig.4) . Each precipitation event coincides with apparent uplift motion in the bias time-series. (Bottom) Coherence time-series with regard to a dry reference date Nov 10, 2014 (gray triangles) and a wet reference date Feb 3, 2017 (black pluses). The red and the blue lines are the dry and wet coherence time-series respectively after medium filtering.

response (relative to the reference pixel) to the same drying process after precipitation.

IX. Conclusions

We present a model for multi-looked interferometric phase that can consistently explain both closure phase errors and discrepancies between DSI and PSI time-series. In a multi-look window where there are more than one group of measurements, all groups contribute to the multi-looked phase. The weight of each group is decided by the weight of their respective amplitude among all groups. If a temporally inconsistent process has decaying amplitudes either due to relative loss of correlation (comparing to other groups) or shrinking of effective areas, signal associated with the temporally inconsistent process appears as a *fading signal* in time-series. If the primary interest is surface ground displacement measurement, the impact of these temporally inconsistent processes can lead to biased interpretations. We show that sequential closure phases can be used to identify, reconstruct and ultimately correct the bias time-series from DSI time-series. Specifically, we conclude that:

1) Phase changing physical processes with varying amplitude representation in time are temporally inconsistent and cause the presence of non-zero closure phase and *bias* in InSAR time-series.

2) We have developed algorithms for easy identification of areas susceptible to bias, as well as for predicting and correcting bias from InSAR time-series.

3) Depending on the decay rate of the bias, a small-baseline analysis may not have significant bias in some cases (e.g., the bw-10 analysis in Section VII shows negligible bias presence) while in other cases a full-bandwidth analysis may still contain bias (e.g., Fig. 1(a)).

4) The bias time-series of a pixel on the edge of the Bristol dry lake show clear correlation with precipitation and "may" indicate the InSAR phase response to the drying process of soil after precipitation.

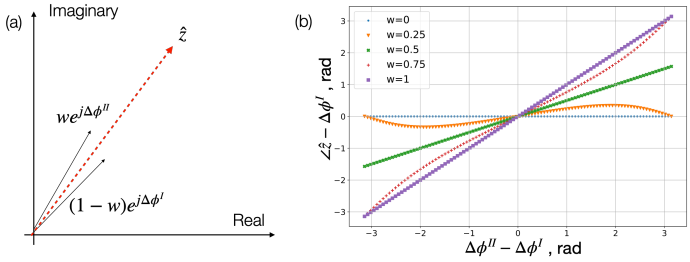

Fig. 10. (a) Illustration of sum of two complex values (b) Illustration of linear approximation when $\Delta\phi^{\mathrm{II}} - \phi^{\mathrm{I}} < 1$ radian

Appendix A
Proof of Equation (9)

$E(\Delta\phi)$ describes the angle of the sum of two complex measurements (Fig. 10(a)) and can be computed using the principles of trigonometry,

$$\begin{aligned} E(\Delta\phi)) &= \angle E(\hat{z}) = \angle\{(1-w)e^{j\Delta\phi^{\mathrm{I}}} + we^{j\Delta\phi^{\mathrm{II}}}\} \\ &= \Delta\phi^{\mathrm{I}} + sin^{-1}(\frac{w}{|\hat{z}|}sin(\Delta\phi^{\mathrm{II}} - \Delta\phi^{\mathrm{I}})) \\ &\approx (1-w)\Delta\phi^{\mathrm{I}} + w\Delta\phi^{\mathrm{II}} \end{aligned}$$

The last equation is derived using small angle approximation. Fig.10 (b) shows that when $|\Delta\phi^{\mathrm{II}} - \Delta\phi^{\mathrm{I}}| < 1$ radian , the above approximation holds.

Appendix B
Simulation when $w_{ij} = w(t_i, t_j)$

In our simulation in Section V, we assume that the physical parameter that describes the temporally inconsistent process increases linearly with time. Here we keep the same parameters in Table. 1 and modify the parameter x so that it contains a non-linear component. We test two scenarios: (1)$x = 0.025\frac{t_i}{\delta_t} + 0.1sin(\frac{\pi}{5}\frac{t_i}{\delta_t})$, and (2) $x = 0.025\frac{t_i}{\delta_t} + 0.5sin(\frac{\pi}{5}\frac{t_i}{\delta_t})$. Fig. 11 illustrates the performances of our algorithms on these two scenarios. When the nonlinear component is relatively small, the proposed algorithm works as expected. When the

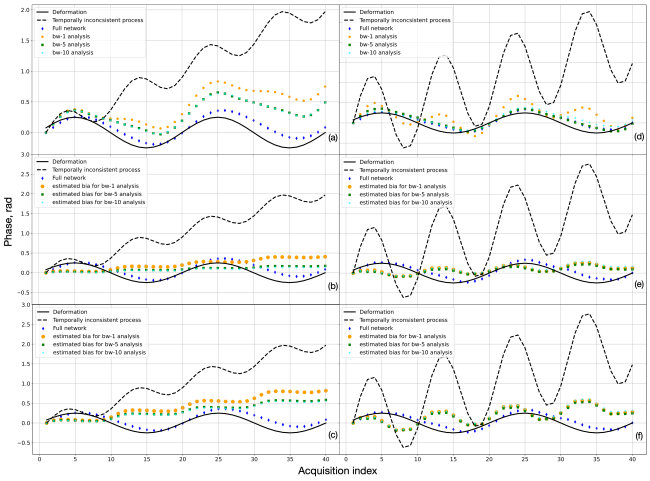

Fig. 11. Same with Fig.1 but with two different configurations of the parameter x. (a)-(c) $x = 0.025\frac{t_i}{\delta_t} + 0.1sin(\frac{\pi}{5}\frac{t_i}{\delta_t})$. (d)-(f)$x = 0.025\frac{t_i}{\delta_t} + 0.5sin(\frac{\pi}{5}\frac{t_i}{\delta_t})$

nonlinear component becomes dominant, the proposed algorithm fails to accurately estimate the bias time-series and the resulting corrected time-series are still diverged.

ACKNOWLEDGMENT

Sentinel-1 data used in this study can be downloaded from https://search.asf.alaska.edu/; The precipitation data can be downloaded from https://www.ncei.noaa.gov/. The research was partly carried out at the Jet Propulsion Laboratory, California Institute of Technology, under a contract with the National Aeronautics and Space Administration. Support was provided from Jet Propulsion Laboratory Advanced Concept funds. The authors would like to thank the anonymous reviewers for their constructive comments that helped improve the manuscript. The authors would like to dedicate this paper to the memory of Michael Rosen, whose work on the Bristol dry lake inspired the choice of the test site used in this work.

REFERENCES

[1] C. Wicks, W. Thatcher, and D. Dzurisin, "Migration of fluids beneath yellowstone caldera inferred from satellite radar interferometry," *Science*, vol. 282, no. 5388, pp. 458–462, 1998.

[2] R. Burgmann, G. Hilley, A. Ferretti, and F. Novali, "Resolving vertical tectonics in the san francisco bay area from permanent scatterer insar and gps analysis," *Geology*, vol. 34, no. 3, pp. 221–224, 2006.

[3] T. Wang, Y. Zheng, F. Pulvirenti, and P. Segall, "Post-2018 caldera collapse re-inflation uniquely constrains kīlauea's magmatic system," *Journal of Geophysical Research. Solid Earth*, 2021.

[4] G. E. Hilley, R. Bürgmann, A. Ferretti, F. Novali, and F. Rocca, "Dynamics of slow-moving landslides from permanent scatterer analysis," *Science*, vol. 304, no. 5679, pp. 1952–1955, 2004.

[5] R. Lanari, F. Casu, M. Manzo, and P. Lundgren, "Application of the sbas-dinsar technique to fault creep: A case study of the hayward fault, california," *Remote Sensing of Environment*, vol. 109, no. 1, pp. 20–28, 2007.

[6] J. Hoffmann, H. A. Zebker, D. L. Galloway, and F. Amelung, "Seasonal subsidence and rebound in las vegas valley, nevada, observed by synthetic aperture radar interferometry," *Water Resources Research*, vol. 37, no. 6, pp. 1551–1566, 2001.

[7] J. Chen, R. Knight, and H. A. Zebker, "The temporal and spatial variability of the confined aquifer head and storage properties in the san luis valley, colorado inferred from multiple insar missions," *Water Resources Research*, vol. 53, no. 11, pp. 9708–9720, 2017.

[8] W. R. Neely, A. A. Borsa, J. A. Burney, M. C. Levy, F. Silverii, and M. Sneed, "Characterization of groundwater recharge and flow in california's san joaquin valley from insar-observed surface deformation," *Water resources research*, vol. 57, no. 4, 2021.

[9] Y. Zheng, H. Zebker, and R. Michaelides, "A new decorrelation phase covariance model for noise reduction in unwrapped interferometric phase stacks," *IEEE Transactions on Geoscience and Remote Sensing*, pp. 1–10, 2021.

[10] P. Agram and M. Simons, "A noise model for insar time series," *Journal of Geophysical Research: Solid Earth*, vol. 120, no. 4, pp. 2752–2771, 2015.

[11] H. A. Zebker, P. A. Rosen, and S. Hensley, "Atmospheric effects in interferometric synthetic aperture radar surface deformation and topographic maps," *Journal of geophysical research: solid earth*, vol. 102, no. B4, pp. 7547–7563, 1997.

[12] T. Emardson, M. Simons, and F. Webb, "Neutral atmospheric delay in interferometric synthetic aperture radar applications: Statistical description and mitigation," *Journal of Geophysical Research: Solid Earth*, vol. 108, no. B5, 2003.

[13] A. Hooper, H. Zebker, P. Segall, and B. Kampes, "A new method for measuring deformation on volcanoes and other natural terrains using insar persistent scatterers," *Geophysical research letters*, vol. 31, no. 23, 2004.

[14] P. Shanker and H. Zebker, "Persistent scatterer selection using maximum likelihood estimation," *Geophysical Research Letters*, vol. 34, no. 22, 2007.

[15] J. Tough, D. Blacknell, and S. Quegan, "A statistical description of polarimetric and interferometric synthetic aperture radar data," *Proceedings of the Royal Society of London. Series A: Mathematical and Physical Sciences*, vol. 449, no. 1937, pp. 567–589, 1995.

[16] P. Berardino, G. Fornaro, R. Lanari, and E. Sansosti, "A new algorithm for surface deformation monitoring based on small baseline differential sar interferograms," *IEEE transactions on geoscience and remote sensing*, vol. 40, no. 11, pp. 2375–2383, 2002.

[17] A. M. Guarnieri and S. Tebaldini, "Hybrid cramér–rao bounds for crustal displacement field estimators in sar interferometry," *IEEE signal processing letters*, vol. 14, no. 12, pp. 1012–1015, 2007.

[18] A. M. Guarnieri and S. Tebaldini, "On the exploitation of target statistics for sar interferometry applications," *IEEE Transactions on Geoscience and Remote Sensing*, vol. 46, no. 11, pp. 3436–3443, 2008.

[19] A. Ferretti, A. Fumagalli, F. Novali, C. Prati, F. Rocca, and A. Rucci, "A new algorithm for processing interferometric data-stacks: Squeesar," *IEEE Transactions on Geoscience and Remote Sensing*, vol. 49, no. 9, pp. 3460–3470, 2011.

[20] P. Shanker, F. Casu, H. A. Zebker, and R. Lanari, "Comparison of persistent scatterers and small baseline time-series insar results: A case study of the san francisco bay area," *IEEE Geoscience and Remote Sensing Letters*, vol. 8, no. 4, pp. 592–596, 2011.

[21] T. R. Lauknes, J. Dehls, Y. Larsen, K. A. Høgda, and D. J. Weydahl, "A comparison of sbas and ps ers insar for subsidence monitoring in oslo, norway," in *Fringe 2005 Workshop*, vol. 610, 2006.

[22] H. Ansari, F. De Zan, and A. Parizzi, "Study of systematic bias in measuring surface deformation with sar interferometry," *IEEE Transactions on Geoscience and Remote Sensing*, pp. 1–1, 2020.

[23] F. De Zan, M. Zonno, and P. López-Dekker, "Phase inconsistencies and multiple scattering in sar interferometry," *IEEE Transactions on Geoscience and Remote Sensing*, vol. 53, no. 12, pp. 6608–6616, 2015.

[24] Y. E. Molan, Z. Lu, and J.-W. Kim, "Influence of the statistical properties of phase and intensity on closure phase," *IEEE Transactions on Geoscience and Remote Sensing*, 2020.

[25] S. Zwieback, X. Liu, S. Antonova, B. Heim, A. Bartsch, J. Boike, and I. Hajnsek, "A statistical test of phase closure to detect influences on dinsar deformation estimates besides displacements and decorrelation noise: Two case studies in high-latitude regions," *IEEE Transactions on Geoscience and Remote Sensing*, vol. 54, no. 9, pp. 5588–5601, 2016.

[26] R. J. Michaelides, H. A. Zebker, and Y. Zheng, "An algorithm for estimating and correcting decorrelation phase from insar data using closure phase triplets," *IEEE Transactions on Geoscience and Remote Sensing*, vol. 57, no. 12, pp. 10 390–10 397, 2019.

[27] J.-S. Lee, K. W. Hoppel, S. A. Mango, and A. R. Miller, "Intensity and phase statistics of multilook polarimetric and interferometric sar imagery," *IEEE Transactions on Geoscience and Remote Sensing*, vol. 32, no. 5, pp. 1017–1028, 1994.

[28] D. Just and R. Bamler, "Phase statistics of interferograms with applications to synthetic aperture radar," *Applied optics*, vol. 33, no. 20, pp. 4361–4368, 1994.

[29] S. Zwieback and F. J. Meyer, "Repeat-pass interferometric speckle," *IEEE Transactions on Geoscience and Remote Sensing*, pp. 1–15, 2020.
[30] M. Manunta, C. De Luca, I. Zinno, F. Casu, M. Manzo, M. Bonano, A. Fusco, A. Pepe, G. Onorato, P. Berardino *et al.*, "The parallel sbas approach for sentinel-1 interferometric wide swath deformation time-series generation: algorithm description and products quality assessment," *IEEE Transactions on Geoscience and Remote Sensing*, vol. 57, no. 9, pp. 6259–6281, 2019.
[31] F. Falabella, C. Serio, G. Masiello, Q. Zhao, and A. Pepe, "A multigrid insar technique for joint analyses at single-look and multi-look scales," *IEEE Geoscience and Remote Sensing Letters*, vol. 19, pp. 1–5, 2021.
[32] M. R. Rosen and J. K. Warren, "The origin and significance of groundwater-seepage gypsum from bristol dry lake, california, usa," *Sedimentology*, vol. 37, no. 6, pp. 983–996, 1990.
[33] M. R. Rosen, "Sedimentologic and geochemical constraints on the evolution of bristol dry lake basin, california, usa," *Palaeogeography, Palaeoclimatology, Palaeoecology*, vol. 84, no. 1-4, pp. 229–257, 1991.
[34] M. R. Rosen, L. L. Stillings, T. Kane, K. Campbell, M. Vitale, and R. Spanjers, "Li and ca enrichment in the bristol dry lake brine compared to brines from cadiz and danby dry lakes, barstow-bristol trough, california, usa," *Minerals*, vol. 10, no. 3, 2020. [Online]. Available: https://www.mdpi.com/2075-163X/10/3/284
[35] Chen and H. A. Zebker, "Two-dimensional phase unwrapping with use of statistical models for cost functions in nonlinear optimization," *JOSA A*, vol. 18, no. 2, pp. 338–351, 2001.
[36] Z. Yunjun, H. Fattahi, and F. Amelung, "Small baseline insar time series analysis: Unwrapping error correction and noise reduction," *Computers Geosciences*, vol. 133, p. 104331, 2019. [Online]. Available: https://www.sciencedirect.com/science/article/pii/S0098300419304194
[37] J. Ruch, J. Warren, F. Risacher, T. R. Walter, and R. Lanari, "Salt lake deformation detected from space," *Earth and Planetary Science Letters*, vol. 331, pp. 120–127, 2012.
[38] P. A. Rosen, M. R. Rosen, and C. J. Rosen, "Exploring the relationship of groundwater exploitation and variability in chemical composition in bristol, cadiz, and danby dry lakes, california," in *AGU Fall Meeting Abstracts*, vol. 2020, 2020, pp. H011–0011.
[39] H. Fattahi, P. S. Agram, E. Tymofyeyeva, and D. P. Bekaert, "Fringe; full-resolution insar timeseries using generalized eigenvectors," in *AGU Fall Meeting Abstracts*, vol. 2019, 2019, pp. G11B–0514.
[40] A. Benoit, B. Pinel-Puysségur, R. Jolivet, and C. Lasserre, "Corphu: an algorithm based on phase closure for the correction of unwrapping errors in sar interferometry," *Geophysical Journal International*, vol. 221, no. 3, pp. 1959–1970, 2020.
[41] C. De Luca, F. Casu, M. Manunta, G. Onorato, and R. Lanari, "Comments on "study of systematic bias in measuring surface deformation with sar interferometry"," *IEEE Transactions on Geoscience and Remote Sensing*, pp. 1–5, 2021.
[42] A. Pepe, Y. Yang, M. Manzo, and R. Lanari, "Improved emcf-sbas processing chain based on advanced techniques for the noise-filtering and selection of small baseline multi-look dinsar interferograms," *IEEE Transactions on Geoscience and Remote Sensing*, vol. 53, no. 8, pp. 4394–4417, 2015.
[43] T. E. Jordan, R. B. Lohman, L. Tapia, M. Pfeiffer, C. P. Scott, R. Amundson, L. Godfrey, and R. Riquelme, "Surface materials and landforms as controls on insar permanent and transient responses to precipitation events in a hyperarid desert, chile," *Remote Sensing of Environment*, vol. 237, p. 111544, 2020.

Yujie Zheng received the B.S. degree from Peking University, Beijing, China, in 2014, and the Ph.D. degree in Geophysics from Stanford University, CA, USA, in 2020. She is currently a Postdoctoral Scholar in the Seismological Laboratory, California Institute of Technology. Her main research interests are Interferometric synthetic aperture radar (InSAR) processing and InSAR applications in crustal deformation studies – earthquakes, volcanoes, anthropogenic signals of deformation such as water management or oil and gas resources.

Heresh Fattahi (M'12) received the M.S. degree in remote sensing engineering from the K. N. Toosi University of Technology, Tehran, Iran, in 2007, and the Ph.D. degree in geosciences from the University of Miami, Coral Gables, FL, USA, in 2015.,He was a Postdoctoral Scholar at the California Institute of Technology from 2015 until June 2017. Since then he has joined the Radar Algorithms and Processing Group, Jet Propulsion Laboratory, Pasadena, CA, USA. His research interests include algorithm development for SAR, InSAR, and InSAR time-series analysis.

Piyush Agram received the B.Tech. degree in electrical engineering from IIT Madras, Chennai, India, in 2004, and the Ph.D. degree in electrical engineering from Stanford University, Stanford, CA, USA, in 2010.,He was a Keck Institute of Space Studies Postdoctoral Scholar with the Caltech's Seismological Laboratory, Pasadena, CA, USA, until 2013 and then joined the Radar Algorithms and Processing Group, Jet Propulsion Laboratory (JPL), Pasadena, CA, USA. In 2020, He joined Descartes Labs as a geospatial data engineer. His research interests include algorithm development for synthetic aperture radar (SAR) focusing, radar interferometry for deformation time-series applications and geospatial big data analysis.

Mark Simons received the B.Sc. degree in geophysics and space physics from the University of California at Los Angeles, Los Angeles, CA, USA, in 1989, and the Ph.D. degree in geophysics from the Massachusetts Institute of Technology, Cambridge, MA, USA, in 1996.,He has been with the California Institute of Technology, Pasadena, CA, USA, since 1996, where he is the John W. and Herberta M. Miles Professor of geophysics with the Seismological Laboratory, Division of Geological and Planetary Science. He is also the Chief Scientist of the Jet Propulsion Laboratory. His research interests include processes associated with the seismic cycle, migration of magma and water in the subsurface, tides, and glacial rebound; tectonics and the relationship between short and long time-scale processes; glaciology, particularly basal mechanics and ice rheology; tools and applications using space geodesy, particularly Global Navigation Satellite System (GNSS) and SAR; Bayesian methods for large geophysical inverse problems; and application of space geodesy for monitoring and rapid response to natural disasters.,Dr. Simons is a fellow of the American Geophysical Union.

Paul Rosen (S/'78, M/'03, SM/'05, F/'10) received a PhD in Electrical Engineering from Stanford University and his M.S. and B.S in Electrical Engineering from University of Pennsylvania. He is currently Project Scientist for NASA-ISRO synthetic aperture radar mission (NISAR) at the Jet Propulsion Laboratory, California Institute of Technology (Caltech). He is also the study coordinator for NASA's Surface Deformation and Change Decadal Survey Architecture Study. His assignments at JPL have encompassed scientific and engineering research and development of radar instruments and applications, as well as technical, organizational and programmatic management of radar developments at JPL. Dr. Rosen is a visiting faculty member at the Division of Geological and Planetary Sciences at Caltech, and has authored on over 40 journal and book chapter publications, and over 100 conference papers. He currently serves as the IEEE Geoscience and Remote Sensing Society Director for Global Activities.